Observations of a tidal intrusion front in a tidal channel

Shasha Lu[a,*], Xiaoming Xia[a], Charlie E.L. Thompson[b], Zhenyi Cao[a], Yifei Liu[a]

[a] Second Institute of Oceanography, SOA, No.36 Baochubei Road, Hangzhou, 310012, China, lss003629@sio.org.cn

[b] Ocean and Earth Science, University of Southampton, National Oceanography Centre, Southampton, Waterfront Campus, European Way, Southampton SO143ZH, UK

Abstract:

A visible front indicated by a surface colour change, and sometimes associated with foam or debris lines, was observed in a tidal channel during neap tide. This is an example of a tidal intrusion front occurring in the absence of sudden topographical changes or reversing flows, typically reported to be associated with such fronts. Detailed Acoustic Doppler Current Profiler and conductivity/temperature/depth measurements were taken on repeated transects both with fronts apparent and with fronts absent. The results indicated that the front occurred as a result of stratification, which was sustained by the buoyancy flux and the weak tide-induced mixing during neap ebb tide. The stronger tide-induced mixing during spring tide restrained stratification, leading to the absence of a front. The mechanism of the frontogenesis was the density gradient between the stratified water formed during neap ebb tide, and the more mixed seawater during neap flood tide; thus, the water on the landward (southwestern) side of the front was stratified, and that on the seaward side (northeastern) of the front was vertically well mixed. Gradient Richardson number estimates suggest that the flow between the stratified and mixed water was near the threshold 0.25 for shear instability. Meanwhile, the density gradient would provide an initial baroclinic contribution to velocity convergence, which is indicated by the accumulation of buoyant matter such as foam, grass, and debris into a sharply defined line along the surface. The front migrates with the flood current, with a local maximum towards the eastern side of the channel, leading to an asymmetrical shape with the eastern side of the front driven further into the Tiaozhoumen tidal channel.

Keywords: tidal intrusion front; tidal channel; stratification; mixing; tidal front asymmetry

1. Introduction

Tidal intrusion fronts are often formed when dense water flows into a basin of less dense water and retains its character as a separate, underflowing dense layer (Largier, 1992). Take an estuary for example, a tidal intrusion front is formed when the tidal inflow of dense seawater floods and prevents a simultaneous buoyant outflow in or near the estuary mouth during flood tide (Thain et al., 2004; Uncles, 2011). The fronts are often visible at the surface due to the presence of debris and foam caused by the strong surface convergence, or/and colour differences between the marine and estuarine water masses along the plunge line (Largier,1992).

These fronts have been observed in many estuaries around the world, including Port Hacking Estuary in Australia, the Palmiet and Qora estuaries in southern Africa, and the Dart estuary in the UK. Most of them are associated with morphological features consisting of a large and sudden change in depth or width (Clifton, 1973; Huzzey, 1982; Largier, 1986; Largier and Taljaard, 1991; Uncles et al., 1997; Thain et al, 2004; Booth, 1987). Brubaker and Simpson (1999) gave a schematic figure of a tidal intrusion front associated with a depth increase. When the tidal flood current flows over the sill, the inflow undergoes a hydraulic jump due to the change in depth, which decelerates the flow. At this point, the inflow no longer has sufficient velocity to resist the outflow and the flow stratifies, resulting in the formation of a front. For this type of tidal intrusion front, it is the topography associated with regions of minimal channel cross sectional area, such as a sill or width constriction, which triggers their formation. For more details, see Brubaker and Simpson (1999). The dynamics of these types of fronts have been successfully described by the internal hydraulic theory of Famer and Armi (1986) and Armi and Farmer (1986).

However, tidal intrusion fronts do not always depend on a controlling morphological feature. An example has been described by Simpson and Nunes (1981) in the Seiont River of

North Wales, UK. Here, when the flood tide flows in, the surface flow on either side of the water mass moves in a reversing direction towards it, resulting in a front. A significant feature of this type of front is a characteristic "V" formation at the surface and a strong point convergence at its apex. For more details of this tidal intrusion front see Simpson and Nunes (1981).

In this study, a tidal intrusion front was observed in a tidal channel, which is not related to a constriction as in the first category of tidal intrusion described above, or following the characteristic shape of the latter one. When the front was present, sampling with an Acoustic Doppler Current Profiler (ADCP) on repeated transects across the front, and conductivity/temperature/depth (CTD) station sampling provided information on the structure of the flow field and density distribution near the front. Additionally, when the front was absent, repeated transects in the Tiaozhoumen tidal channel were undertaken and showed that this tidal intrusion front is strongly associated with stratification during the neap-spring transition.

2. Study area

2.1 Topography

Tiaozhoumen Channel is located between the islands of Liuheng and Xiazhi, in Zhejiang Province, China (Fig. 1). The southwestern side of the channel is the coastline of Liuheng Island, while the northeastern side of the channel are open to several entrances to the Xiazhimen Channel. Based on bathymetric data, the channel can be divided into three segments according to their topographic features. First, in the lower channel segment there are a large number of islands. The terrain here is irregular, and the channel has several entrances. Second, the middle channel is relatively flat, with 10-20 m depth contours running approximately parallel to the coastline, and reaching a maximum depth of 30m. Third, in the upper channel segment there are many reefs and shoals, and the underwater topography is irregular. The main channel in this segment shows a north-south direction, inconsistent with

the shore-parallel channel in other segments. Therefore, the tidal channel in this study area forms a bend, keeping parallel to the shoreline of Liuheng Island.

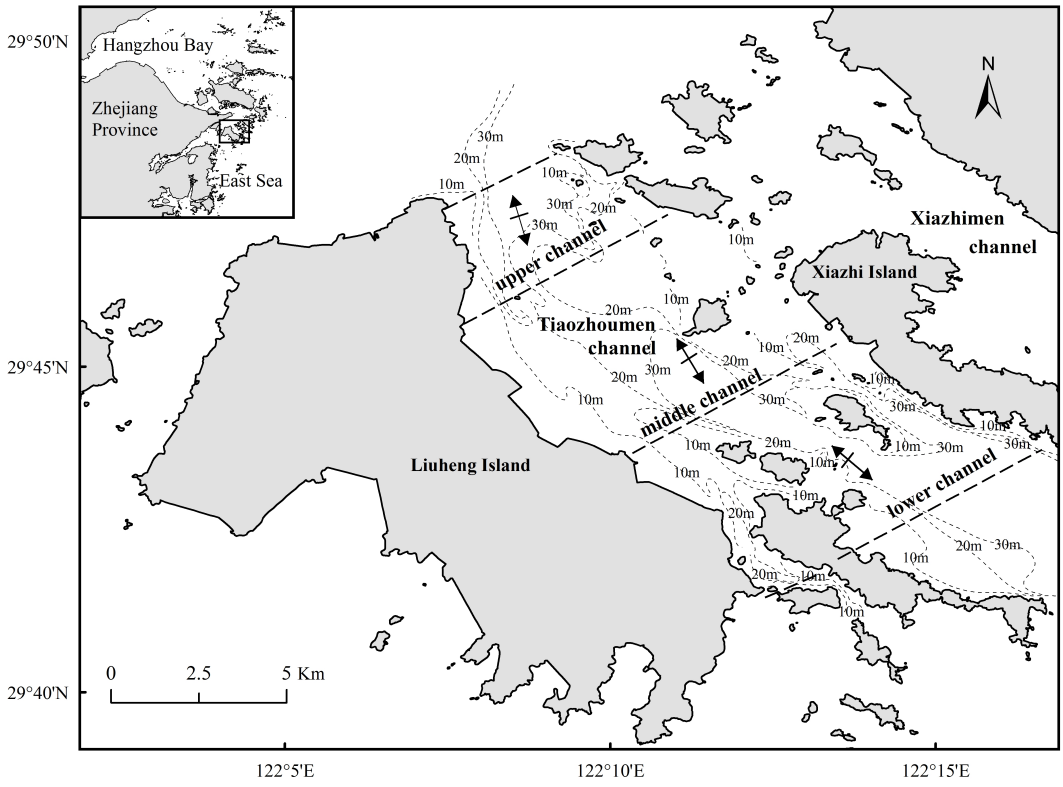

Fig. 1. The study site of Tiaozhoumen tidal channel, in the lower channel segment there are several islands and a rotation of the flow, in the middle channel segment the topography is flat and the flow is reciprocating, in the upper channel segment there are many reefs and shoals, with a predominantly reciprocating flow.

2.2 Oceanography

A number of recent studies investigating currents through Tiaozhoumen Channel have been undertaken by the Second Institute of Oceanography, State Oceanic Administration, China (e.g. Li et al., 1994; Yang et al., 2004). Based on the observational data accumulated since 1994, the general oceanographic setting of the study area is described as follows:

The flow in the tidal channel is dominated by semi-diurnal tidal currents. The study area has a variable spring-neap tidal range, with a 3.1 m mean spring range and a 1.4 m mean neap range. Waves are not significant for most of the year, with a mean wave height of 0.3 m,

increasing to 2.5 m only under typhoon conditions (usually between July-September) (Li et al., 1994).

The current flow is affected by the local topography and shoreline morphology. In general, reciprocating flows dominate in the main channel, but in the lower channel segment, the appearance of a number of islands results in a characteristic flow rotation. The flow directions in the upper, middle and lower channel segments differ as a result of the curvature of the coastline of Liuheng Island, as shown in Fig. 1. The current flows faster on the northeastern side of the channel than the southwestern (shallower) side due to differences in depth. In addition, the connection with the Xiazhimen Channel may bring the flood current from Xiazhimen Channel to Tiaozhoumen Channel, resulting in a flood current that is faster to the eastern side of the middle channel (Yang et al., 2004).

Lastly, the flood currents come from the open sea with high salinity and low sediment concentration, while the ebb currents originate from Hangzhou Bay. The ebb currents therefore have low salinity and high sediment concentration compared to the flood currents. Consequently, differences in both salinity and sediment concentration occur between the flood and ebb currents.

3. Methods and data collection

In this survey, water velocity and water property (temperature, salinity, and turbidity) profile data were collected using a vessel with a length of 53.5 m and a width of 9.2 m. In addition, two satellite image maps with observable frontal lines are presented.

3.1 Observation instruments

The velocity data were collected using an RD Instruments 600 kHz downward-looking, vessel-mounted ADCP. The vertical resolution was 1 m and the sampling frequency was 1.3 Hz. The vessel was accurately located through Differential Global Positioning System (GPS) equipped real-time positioning and mapping software. Profiles of water temperature, salinity,

and turbidity were collected using a XR-620 CTD. The temperature and salinity data are obtained directly from the CTD output, while the suspended sediment concentration (SSC) data are calculated from instantaneous turbidity measured by the turbidity sensor in the CTD. In this paper, a simple linear regression is developed to estimate the relationship between turbidity and SSC through laboratory calibration (Fig. 2), and this is used to calculate the instantaneous SSC. The CTD is installed on a manual winch on the vessel deck, with a sampling frequency of 6 Hz and an average depth resolution of approximately 0.1 m.

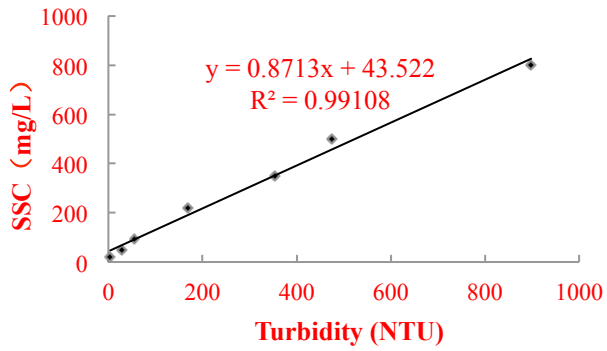

Fig. 2. The relationship between turbidity and SSC. Abscissa is the turbidity value provided by the CTD, and ordinate is the SSC value measured in the laboratory with the same seawater sample. The black points represent the measured values. The solid line represents the linear regression, SSC=0.8713*turbidity+43.522, with an R-squared of 0.9911.

3.2 Observation range

Due to government waterway control and the pressure/depth limitations of the instruments, the middle tidal channel with its relatively flat bathymetry was selected as the observational region. Two cruises were carried out under varying tidal regimes, one during neap tide (27 May 2015) and one during spring tide conditions (1 June 2015). Sampling observations on both cruises were carried out during a 13-h window from 5:00 to 18:00 Beijing local time (UTC +08:00), as shown in Fig. 3.

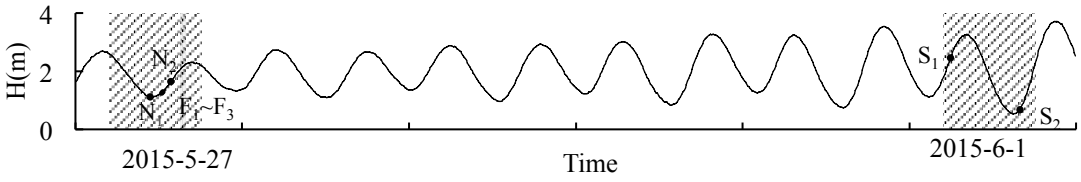

Fig. 3. Schematic of observation periods: the solid line represents the tidal water level (H) and the shaded part represents the sampling observation periods (from 5:00 to 18:00 on 5/27 at neap tide and on 6/1 at spring tide). The grey shading represents the period of mapping the position of the front (from 15:00 to 15:40 on 5/27), while for the rest time the observations of velocity and vertical profiles of temperature, salinity and turbidity were collected (Stations N_1/ N_2 were sampled at 10:38/13:43 on 5/27, S_1/S_2 at 5:51/15:48 on 6/1, F_1/ F_2 / F_3 at 12:09/12:14/12:28 on 5/27).

3.3 Sampling modes

During this study, the front was observed by colour changes, or/and a thin line of foam and accumulated grass and debris. Three types of surveys were undertaken to characterize the front. First, due to the visibility of the front, it was possible to map the front by vessel over a short period of time. By comparing the recorded timing with the GPS records, which included time, latitude, and longitude, the position and shape of the front was recorded. Mapping of the front was undertaken from 15:00 to 15:40 on 27 May (Fig. 3). Second, the intensity of the surface front was evaluated by measuring the horizontal variations of temperature, salinity, and turbidity across the frontal zone using a vessel-towed CTD at an approximate depth of 0.5 m below the water surface. Third, measurements of vertical profiles of temperature, salinity, and turbidity were taken, using a CTD lifted by a hand-operated winch. 105 stations were sampled throughout the survey as shown in Fig. 4, with 38 stations sampled during the neap tide and 67 stations during the spring tide. The station positions were chosen every few hundred metres, on both sides of the visible front. The ADCP recorded data throughout the survey.

3.4 Satellite remote sensing

Due to the high visibility of the frontal line, satellite remote sensing is a viable method for locating the position and shape of the front based on the colour change between clear water and turbid water. Two sets of satellite images were used in this study to identify the frontal position through colour change: Landsat 5TM with a spatial resolution of 30 m taken on 6 July 1990 (curve L1 in Fig. 4); and Landsat 8 with spatial resolution of 15 m on 12 July 2013 (curve L2 in Fig. 4). Due to the Landsat resolution of 15-30 m, which is wider than the width of the front line, front identification only using the satellite remote sensing to observe the colour change between clear water and turbid water is difficult. Therefore, the latitude and longitude data of each point of curves L1 and L2 are not accurate, but the information of the general position and shape of the front can be given.

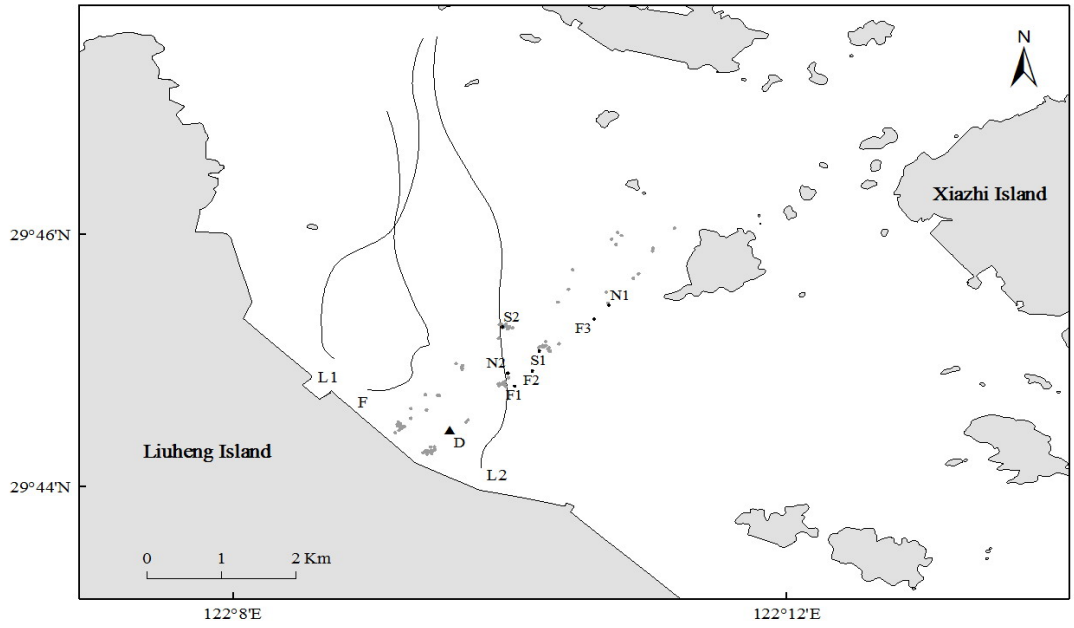

Fig. 4. Station locations and front positions. 105 points represent all stations used for measuring vertical profiles of temperature, salinity and turbidity. Among them, highlighted points N_1 represent for neap ebb tide, N_2 for neap flood tide, S_1 for spring flood tide, S_2 for spring ebb tide, F_1 on the turbid side of the visible front line, and F_2/F_3 on the clear side of the line. The Triangle D represents a continuous observation station for the measurement of temperature, salinity and turbidity and vertical profiles of velocity. Curves F, L1 and L2 indicate the approximate position and shape of the visible frontal line recorded by mapping

the position between 15:00 to 15:40 on 5/27 (F), and located from the satellite images taken on July 6, 1990 (L1) and July 12, 2013 (L2).

4. Results

A visible front was initially observed at approximately 12:00 on 27 May, during the late ebb period of the neap tide (13:30 is the time of slack water before flood tide), but this front line was vague and intermittent, as shown in Fig. 5a. When the tide turned to flood, the frontal boundary became clearer and more stable, identifiable from the lines of colour change, foams and debris, or both, as shown in Fig. 5b. The front moved to the northwest with the flood tidal currents. However, the front was not observed during the spring tidal conditions (1 June). These results agree with the long-term observations of local fishermen.

(a) neap ebb tide (b) neap flood tide

Fig. 5. Photographs of the tidal intrusion front during the neap tide, marked by a colour change and a line of foam. (a) The frontal boundary was indistinct and disappeared occasionally during the neap ebb tide; (b) the frontal line was clear and persisted almost through the whole neap flood tide.

4.1 Horizontal gradient across the frontal zone

A transect was taken using a vessel-towed CTD crossing the front, orthogonal to its surface expression at an approximate depth of 0.5 m below the water surface and with an accuracy of approximately 1 m in the horizontal, to observe the detailed variation of water column

properties across the visible frontal line. This sampling method allowed the accurate calculation of the size of the frontal zone and the horizontal gradient of water properties across the frontal zone.

The observed temperature (T), salinity (Sa) and calculated suspended sediment concentration (SSC) and density across the front are shown in Fig. 6, with the origin assumed to be at the position of the visible front. The results show that SSC, density, temperature, and salinity exhibit strong horizontal gradients across the frontal zone. The SSC reduced from 60 $mg \bullet L^{-1}$ at -10 m to 20 $mg \bullet L^{-1}$ at 10 m over 20 m distance, with a gradient of approximately 2 $mg \bullet L^{-1} \bullet m^{-1}$. The strong gradient of SSC agrees with the colour change seen, with yellow colouration on the landward side of the front and blue on the seaward side. The density increased rapidly from 1018.24 $kg \bullet m^{-3}$ at -55 m to 1018.86 $kg \bullet m^{-3}$ at -45 m over a 10 m distance, with a gradient of approximately 0.062 $kg \bullet m^{-3} \bullet m^{-1}$. This increase was driven by an intense horizontal gradient in salinity of 0.06 m^{-1} in the same area. Differing from the single point of distinct change shown by SSC, density, and salinity, the temperature exhibited two locations with strong horizontal gradients (one is approximately 0.075℃$\bullet m^{-1}$ at -50 m, and the other is approximately 0.04℃$\bullet m^{-1}$ at 0 m).

The span of frontal zone was approximately 60m, from -50m to 10m, marked by sudden changes in salinity, SSC, or temperature. Although it is acknowledged that the intensifications of the horizontal gradients of water properties across the frontal zone were not stationary, this transect provides insight into the magnitude of intensity/span of this front, and the variation in the horizontal direction of the water properties at the local frontal zone.

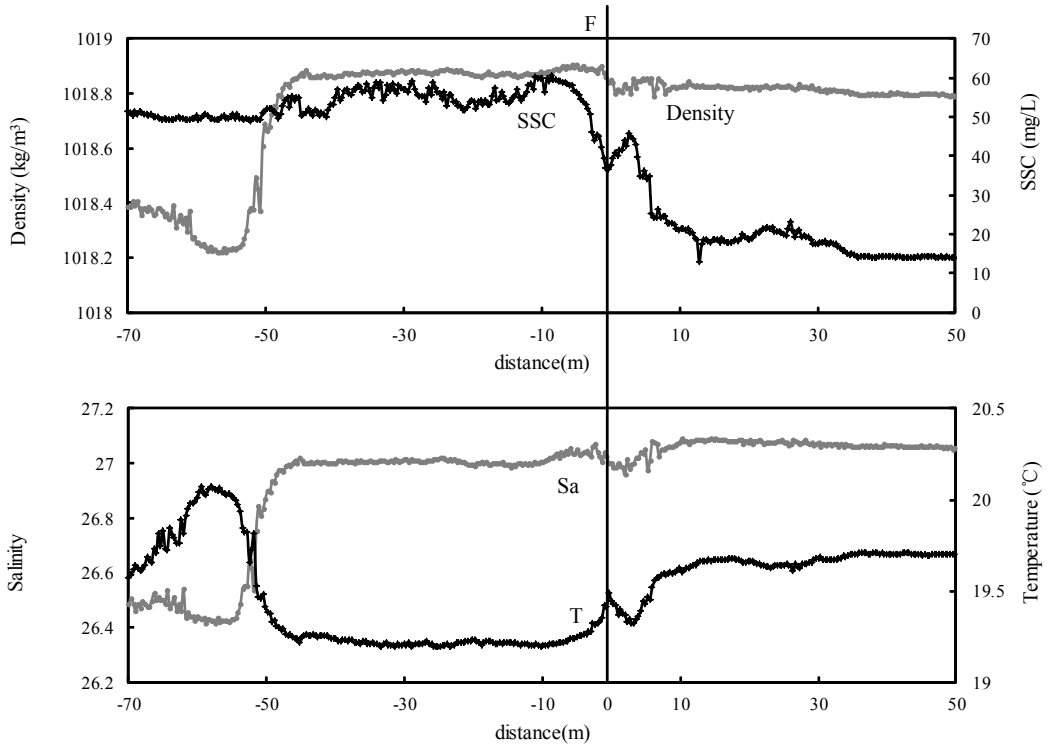

Fig. 6. Density, SSC, temperature, and salinity of the surface layer across the frontal zone, where the origin is assumed to be at the position of the visible frontal line marked by colour change (indicated by the symbol "F", with yellow colouration on the southwestern side of the front and blue on the northeastern side)

4.2 Vertical structure on two sides of the front

Three pairs of stations on either side of the visible front were sampled with vertical profiles of water column temperature, salinity, and turbidity; additionally, the velocity fields on both sides of the front were obtained. One data pair, F_1 and F_2/F_3 (position shown in Fig. 4), is presented here, as a representative of the two water masses on the each side of the front. A sharp, visible frontal boundary marked by a colour change was observed between stations F_1 and F_2/F_3 at the time of sampling, with the turbid water at station F_1 and clear water at stations F_2/F_3.

The vertical profile of salinity, SSC, and temperature on the opposite sides of the front at stations F_1 and F_2/F_3 are illustrated in Fig. 7. The vertical temperature structure at all stations

consisted of two distinct layers due to solar heating, with a higher temperature layer found at depths shallower than 5 m overlaying a lower-temperature layer. However, the temperature difference is small, indicating a negligible contribution to the density variation. Therefore, the density variation here was dominated by salinity differences. There was a similar variation in the trends of salinity and SSC. On the turbid side of the front, at station F_1, the water column was clearly stratified, with a gross structure consisting of two distinct, nearly homogeneous layers. The interface of the pycnocline separating the two layers was sharp, with the gradient occurring at approximately 5 m in the vertical. The salinity increased 0.6 from a water depth of 3.8 m to 5.2 m, while the SSC increased 80 kg/m^3 for the interface from water depth of 2.2 m to 5.7 m. In contrast, on the clear (seaward) side of the front, at station F_2, the water column showed greater mixing, and the pycnocline broadened considerably. The salinity gradient increased from a depth of 1.5 m to 24 m, and the SSC increased from 3.5 m to 16 m. Farther away from the front, at station F_3, the water column was well mixed.

Comparing the two sides of the front, the SSC at station F_1 was greater than that at station F_2, agreeing with the observed colour change. The salinity at station F_1 was lower than that at station F_3, in agreement with the general trend of ebb currents having low salinity and flood currents having high salinity. However, the salinity at station F_2 was lower than that at station F_1, which was expected to be higher because station F_2 was positioned on the seaward side of the front. This distinguishing feature of the salinity variation is also observed in the horizontal variation of surface salinity across the frontal zone (Fig. 6), where the surface salinity decreases at the corresponding point of the SSC front. Together, these observations suggest that the salinity ahead of the SSC front would be slightly lower, which may be related to the SSC frontal circulation.

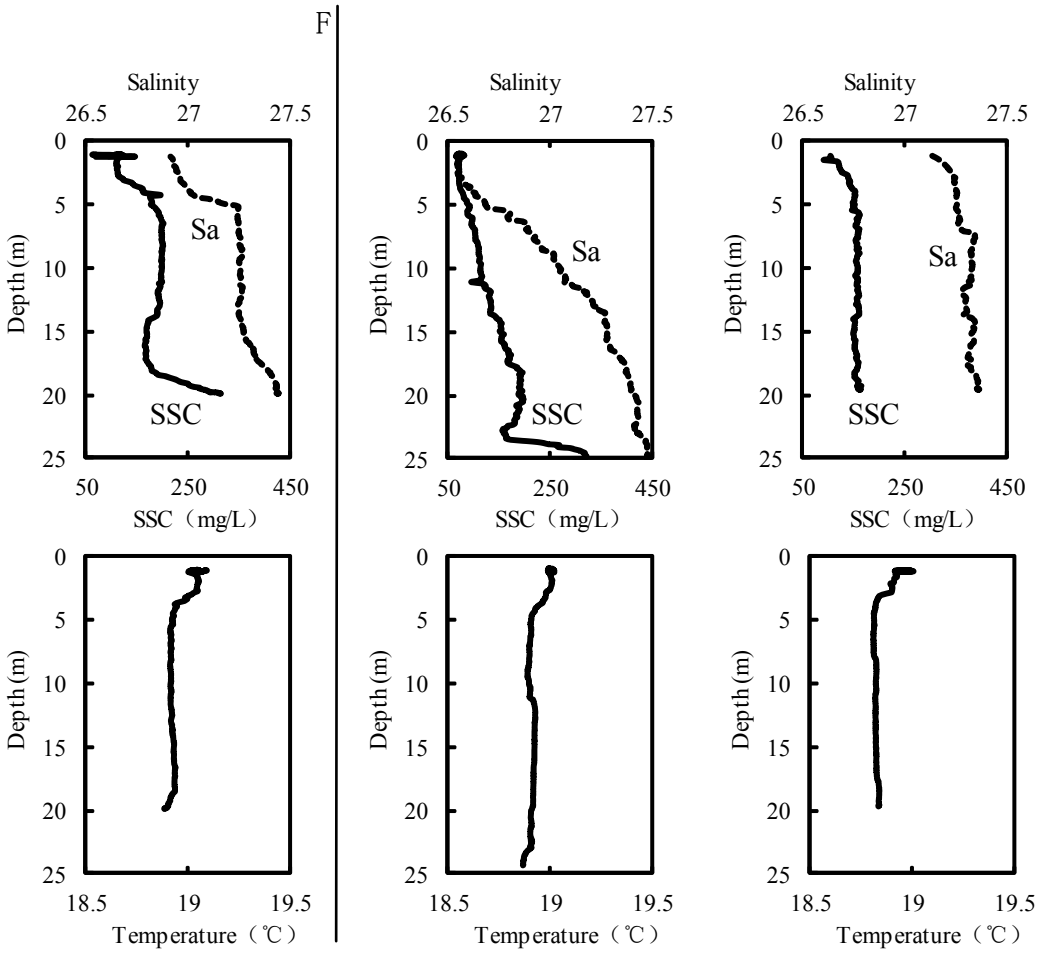

(a) Station F_1 (b) Station F_2 (c) Station F_3

Fig. 7. Observed vertical structure of salinity (Sa), SSC and temperature across the front at stations F_1 and F_2/F_3. In transects where a sharp visible frontal boundary was observed at the surface from colour changes, its correspondence is between F_1 and F_2, with F_1 on the turbid (landward) side and F_2 on the clear (seaward) side.

4.3 Velocity field in the frontal zone

A complete view of the 10-s average velocity magnitude acquired during the cross-front cast between stations F_1 and F_2 is provided in Fig. 8, as sets of sequential ADCP ensembles sampled. Each individual 10-s ensemble represents an average over a horizontal interval of approximately 20 m at a vessel speed of approximately 2 $m \cdot s^{-1}$. This vector represents the velocity component orthogonal to the line of the front.

The visible frontal line (as indicated by the symbol "F" in the vector plot) is located between ensembles 40 and 50. Before approaching the front, the current between ensembles 10 and 40 exhibited typical tidal flow profile, with the maximum speed at the surface. Maximum speeds were approximately 79 cm•s^{-1} on ensemble 40. On crossing the front, the flow was obstructed, and the flow velocity decreased rapidly, especially in the surface layer. Maximum speeds were approximately 24 cm•s^{-1} on ensemble 50, reduced by 55 cm•s^{-1} compared with ensemble 40. This velocity structure was observed to persist over the next 60 m, spanning ensembles 50-70. This zone coincides with the frontal zone as marked by the sudden change of the water properties in Section 4.1. After crossing the frontal zone, the structure of the velocity field returned to the typical tidal flow profile on the seaward side of the front. In spite of these magnitude differences, the flows on both sides of the front moved in the same direction.

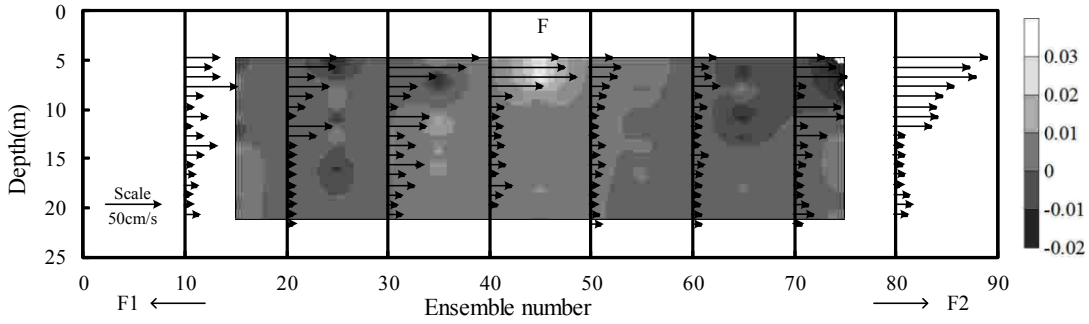

Fig. 8. Vector plots representing the 10-s average ADCP data acquired during the cross-front casts between stations F_1 and F_2. Each individual 10-s ensemble represents an average over a horizontal interval of approximately 20m at a vessel speed of approximately 2m•s^{-1}. Colour grade represents the convergence of the across-front velocity gradient fields. The surface expression of the visible frontal boundary is indicated by the symbol "F".

The gradient of the across-front velocity $-\partial u/\partial x$ is shown in Fig. 8, which is a finite difference estimation based on consecutive ADCP ensembles. A prominent zone of intensified convergence was observed at the front near the top of the ADCP profiling range between ensembles 40 and 50. The accumulation of buoyant matter such as foam, grass, and

debris into a sharply defined line at the surface are visible indicators of surface convergence, as well.

4.4 Shape of the visible frontal surface

From 15:00 pm to 15:40 pm on 27 May 2015, the front migrated to the northwest with the flood tidal currents. We tracked the visible front from its coherent frontal boundary, as introduced in Section 3.3. The shape of the front was delineated by the visible line at the surface and is represented by curve F in Fig. 4. The front can be tracked from the shallow side of the channel to the deeper side, curving in the northeast direction with a distinctive shape, which was also seen in the historical satellite data (indicated by curve L1 and L2 in Fig. 4).

5. Discussion

5.1 Stratification, mixing and frontogenesis

The results show that during the neap tide the front formed during the last a few hours of ebb and subsequently moved downstream during the flood, whereas during the spring tide, the front dissipated. This conceptually indicates that the formation, migration, and disappearance of the front were strongly associated with the neap-spring transition. The vertical profiles of water properties (temperature, salinity, and turbidity) at 105 stations during neap and spring tides (Fig. 4) are shown in Fig. 8, using representative profiles of salinity during the neap ebb tide (N_1), neap flood tide (N_2), spring flood tide (S_1) and spring ebb tide (S_2). The water column at station N_1 appears clearly stratified during the neap ebb tide, but increased mixing is observed at station N_2 during the neap flood tide. It was well mixed at stations S_1 and S_2 during both the spring ebb and flood tides, indicating that the stratification had a distinct spring-neap cycle.

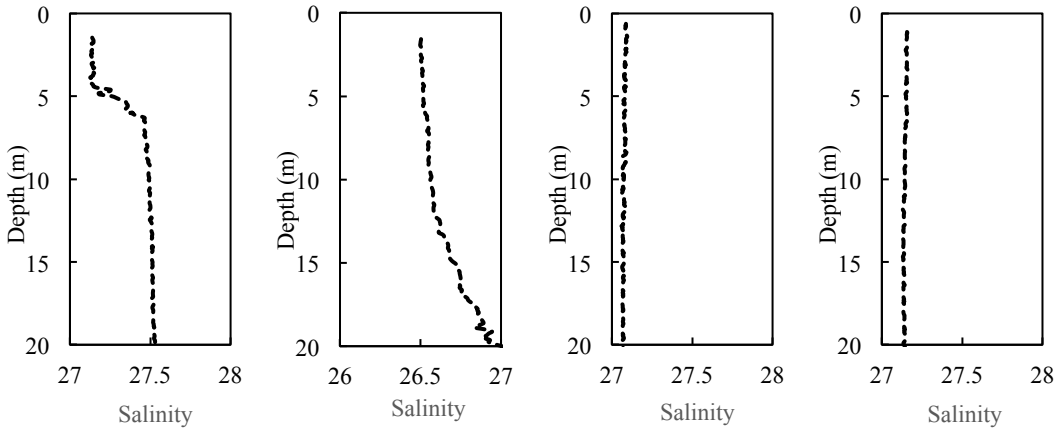

(a) Staion N_1 (b) Staion N_2 (c) Staion S_1 (d) Staion S_2

Fig. 9. Observed vertical structure of salinity at stations representing the four conditions of neap ebb tide (N_1), neap flood tide (N_2), spring flood tide (S_1) and spring ebb tide (S_2). Their sampling times are shown in Fig. 3, and their positons are shown in Fig. 4.

Stratification or mixing is dependent on the magnitude of buoyancy and tide-induced mixing (Simpson and Hunter, 1974; Nunes Vas et al, 1989; Wang ,1998). The criterion $\frac{h}{\overline{u}}$, based on an energy budget argument (Nunes Vas et al, 1989; Wang ,1998) is used to predict the stratification due to the buoyancy flux from fresh water discharges:

$$\frac{h}{\overline{u}} = K\left(\frac{\partial \rho}{\partial x}\right)^{-\frac{1}{2}}$$

where K is a coefficient related to the environment,

$$K = 4\left(\frac{5a_1 C_d \in B^3 {\rho_r}^2}{3\pi g}\right)^{\frac{1}{4}}$$

where h is depth, $\overline{u}$ is mean velocity, ρ is density of seawater, a_1 is an empirical constant relating to the vertical eddy viscosity (0.0012), C_d is a bottom drag coefficient (0.0025), $\in$ is the turbulent mixing efficiency (0.0037), B is a ratio of amplitude of the bottom tidal velocity

to that of the depth average tidal velocity (0.78), ρ_r is mean density of seawater (1025 kg•m^{-3}), and g is acceleration due to gravity (9.8 m•s^{-2}).

As introduced earlier the buoyancy flux in Tiaozhoumen Channel results from the density difference between the ebb water from Hangzhou Bay and the flood water from the sea. Based on the measured data from station D (Fig. 4), the horizontal density gradient $\frac{\partial \rho}{\partial x}$ was calculated as approximately 4.4*10^{-5} kg•m^{-4} during the neap tide, and 6.6*10^{-5} kg•m^{-4} during the spring tide. The corresponding $K\left(\frac{\partial \rho}{\partial x}\right)^{-\frac{1}{2}}$ is calculated to be 42.3 during the neap tide, and approximately 37 during the spring tide. Meanwhile, we select two points from the flat part of the main channel to calculate $\frac{h}{\overline{u}}$ during the spring/neap tide. As the middle channel is flat, velocities in the main channel vary limitedly and the velocity data of these two points are used to represent the velocity of the main channel as a whole. T he water depths of the two selected points are both 30 m, and average velocities are 0.6 m•s^{-1} during neap tide and 0.9 m •s^{-1} during spring tide.Thus

$$\frac{h}{\overline{u}}$$

is calculated to be 50.0 during neap tide (>42.3), indicatin g stratification as shown in Fig. 9(a,b), while it is calculated to be 32.2 during the spring tide (<37), indicating a well-mixed water column as in Fig. 9(c,d). Stratification is considered more likely during spring due to the greater density gradient, but in fact no stratification is observed. This is because the tide-induced mixing during the spring tide is also stronger and breaks down any stratification. It is therefore suggested that the increase of tidal current velocity was the main control on stratification and led to the absence of a front during spring tides. Similarly, the front does not persist under rough seas, which also result in a strong mixing, as noted by local fishermen.

The structure of this tidal intrusion front is similar to a tidal front as described by Simpson and Hunter (1974); however, the causes of mixing are different. Mixing at a tidal front is

caused by tide-induced mixing energy, and $\frac{h}{\overline{u}}$ on either side of the front changes little for some time; therefore, the front is always stationary and exists whether flood or ebb tide is occurring. However, the mixing of the observed tidal intrusion front is caused by the intrusion of flood current waters, leading to the mixing or replacement of the stratified water mass with the mixed flood water; therefore, the front is not stationary and moves in the migration direction of the flood current, and it always appears during neap flood tide.

In this study, when the tidal inflow of dense and mixed water meets the ambient stratified water of less density during flood tide, a front forms. At the seaward of the front, considerable mixing is seen (Fig. 7b, 7c), while on the opposite side of the front, the water column is stratified (Fig. 7a). The threshold between the stratification and mixing will depend on the dynamic stability of the flow, which may be investigated in terms of the gradient Richardson number (Miles, 1961; Hazel, 1972; Erikson, 1978; Abarbanel, 1984)

$$Ri = N^2/S^2$$

where N is the buoyancy frequency, given by $N^2 = (-g/\rho)(\partial\rho/\partial z)$, ρ is density, z is depth, and S is the vertical shear, given by $S^2 = (\partial u/\partial z)^2 + (\partial v/\partial z)^2$, where u and v are the velocity components in the longitudinal and transverse directions.

Miles (1961) provided analytic proof that for $Ri > 0.25$ stability can be assumed, but noted that instability would not necessarily occur for $Ri < 0.25$. Geyer and Smith (1987) suggested that the Richardson number threshold of instability was approximately 0.25 if based on instantaneous shear (including the contribution from internal waves) and approximately 0.33 if based on mean shear (averaged over timescales that are long compared to the buoyancy period, $2\pi/N$), taken from field measurements involving high-resolution velocity and density.

Here, S was determined from a 60-s average of the ADCP data, and N was determined from the CTD cast to determine Ri for stations F_1-F_3, and δ represented the thickness of the

pycnocline (used for the integration of density and velocity). The results are presented in Table 1.

Table 1. Shear Layer Parameters

Station	Time	Pycnocline thickness δ, m	Shear *S*, s^{-1}	Buoyancy frequency *N*, s^{-1}	*Buoyancy Periods,* 2π/N, *s*	*Ri*
F_1	12:09	3	0.114	0.161	39	2.00
F_2	12:14	22	0.130	0.182	35	1.94
F_3	12:46	20	0.112	0.050	126	0.23

In our *Ri* estimation, the 0.25 threshold is probably more appropriate because our shear measurement interval (60s) was not always longer than the buoyancy period (the minimum internal wave period is 126s). The calculated *Ri* results suggest that $Ri < 0.25$ only at station F_3, indicating shear instability, and $Ri > 0.25$ at stations F_1 and F_2, indicating stratification; although not consistent with the position of the front (between stations F_1 and F_2), it is consistent with the measured vertical profiles.

Stratification and the velocity convergence affect the tidal intrusion front simultaneously, and either or both may be the genesis mechanism of the front. In this study, there is no abrupt change in the terrain in the main channel, so the structure of the velocity field exhibits a typical tidal flow profile when no front is present. The velocity convergence occurred only when the front passed. Thus, it might be assumed that the velocity convergence is the result of the front, not the cause of it. The frontogenesis is based on a density gradient between the mixed water mass and the stratified water mass, which is sustained by a buoyancy flux and weak tidal mixing, and would therefore provide an initial baroclinic contribution to velocity convergence.

5.2 Migration of the front

The tidal intrusion front formed due to the intrusion of flood current and migrated with the flood current. The position of the frontal boundary was not stationary. Based on two recorded positions of the observed front, it moved approximately 3 km between 12:00 and 15:00 on 27

May, providing an estimated average frontal migration speed of 0.185 $m \bullet s^{-1}$ during this phase. Moreover, the measured average speed of the ebb flow from 12:00 to 13:30 was approximately 0.125 $m \bullet s^{-1}$, and the measured average speed of the flood flow from 13:00 to 15:00 was approximately 0.313 $m \bullet s^{-1}$. Therefore, the average speed of the flow during the corresponding sampling time was approximately 0.188 $m \bullet s^{-1}$, in agreement with the calculated front migration speed of 0.185 $m \bullet s^{-1}$. The front was therefore moving at the same speed as the tidal flow.

There is an inconsistency with a span of approximately 60 m between the positions of the SSC front (visible) and the temperature/salinity front (non-visible), as shown in Fig. 6. This inconsistency may be explained by turbulence theory. The SSC front is related to the turbulent diffusion of suspended sediment, which is supported by large vortexes, while the temperature/salinity front is related to momentum exchange, which rely on small vortexes. In addition, some laboratory experiments provide evidence that the SSC affects the turbulence exchange. Therefore, the turbulent diffusions of suspended sediment and temperature/salinity are different, thus the positions of their fronts are not coincident.

The tidal intrusion front in this tidal channel has an asymmetrical shape, with an offset of approximately 2500 m between the deeper and shoal side, based on the measured results indicated by curve “F” in Fig. 4. The migration of the frontal zone between 15:00 and 15:40 (the time taken to travel the length of the front during sampling) was approximately 1200 m, with an average speed during the corresponding time of approximately 0.5 $m \bullet s^{-1}$. This confirms that the asymmetrical shape of the frontal line is not just an artefact of the migration of the frontal position over the measurement duration. The satellite images also present similar shapes (indicated by curves L1 and L2 in Fig. 4). According to Largier (1992), two theories may be used to explain this asymmetrical shape. One results from differences in the inflow velocity over the channel and the shoals. Strong bottom friction results in slower currents in shallower regions, and faster currents in the deeper sections (Huzzey and Brubaker,

1988; Li, 2002), which will result in the faster inflowing water pushing ahead farther. In this case, the east side of the channel is deeper, and the flow there is faster. The front on the eastern side is thus driven further down the channel and gives the asymmetrical shape. The other theory is related to the inflow directed towards the coastline as the channel bends. In this case, the tidal channel curves, which results in an off-centre flow towards the east, which has been observed at this site. This effect would also shift the velocity maximum towards the eastern side of the channel, in a similar way to that observed in the Pistol Estuary in Oregon, USA. The particular shoreline of this channel, with one side adjacent to the coastline and one side in open sea with islands, may emphasize the asymmetrical shape. As introduced above, the flood currents in the eastern side of the middle channel also flow faster due to the connection with the Xiazhimen Channel, leading to the front line pushed further landward. Therefore, it is suggested that the particular topography with the presence of the shoals, the curve of the channel, and the connection with the external water, all lead to a local velocity maximum towards the east, which then causes the frontal line to have an asymmetrical shape oriented obliquely across the along-channel flow.

6 Conclusions

During the observation of neap (27 May) and spring (1 June) tides in Tiaozhoumen Channel, a visible front was present during neap tide, identifiable from lines of colour change, foams and debris, or both, but was not observed during spring tidal conditions. The front migrated with the flood tidal current and was stable with a distinct frontal boundary line, as shown in Fig. 5b. These observations are consistent with the observations of local fishermen.

The structure of the frontal zone was analysed with velocity and water property profile data (temperature, salinity, and SSC). The horizontal span of this frontal zone was approximately 60 m, revealed by changes in salinity, SSC, and temperature, as well as the change in the velocity structure (Fig. 6, 8). The vertical structure on either side of the frontal line shows that one side was stratified with a two-layer structure, and the other was well mixed (Fig. 7). The

front had an asymmetrical shape with the eastern side of the channel plunging more, which is also observed from two satellite image maps (Fig. 4).

The observed tidal intrusion front occurs in the absence of sudden topographical changes or reversing flows typically associated with such fronts. The mechanism causing this front was the density gradient between stratified water and mixed water. Stratification depends on the density difference between the ebb water and flood water, and the low tidal power during the neap tide (Fig. 9). Stronger mixing on the seaward side of the front was due to the intrusion of the mixed flood seawater, which led to the mixing or replacement of the stratified water. Therefore, the front was not stationary but instead moved with the flood current.

In addition, the salinity has an abnormal decline at the corresponding point of the SSC front (Fig. 6, 7), which has not been reported by previous studies and warrants further study.

Acknowledgements

This work was supported by the Natural Science Foundation of China (grant Number 41406099). Cai Tinglu and Chen Renzhe assisted in the field data collection, and Li Yan and Jia Jianjun were very generous with their time in discussing the scheme of the fieldwork. Chen Yining provided language assistance.

References

1 Armi, L., Farmer, D.M., 1986. Maximal two-layer exchange through a contraction with barotropic net flow. Journal of Fluid Mechanics 164, 27-51.

2 Bagnold, R.A., 1955. Some flume experiment on large grains but little denser than transporting fluid, and their implications. Proceeding of the Institution of Civil Engineers 4(2), 174-205.

3 Booth, D. A., 1987. Some consequences of a flood tide front in Loch Creran. Estuarine, and Coastal Shelf Science 24(3), 363-375.

4 Brubaker, J.M., Simpson, J.H., 1999. Flow convergence and stability at a tidal estuarine front: Acoustic Doppler current observations. Journal of geophysical research 104(18), 18257-18268.

5 Clifton, H.E., Phillips, R.L., Hunter R.E., 1973. Depositional structures and processes in the mouths of small coastal streams, southwestern Oregon. In: D. R. Coates (ed.), Coastal Geomorphology, Publications in Geomorphology. State University of New York, Bingham, New York, pp. 115-140.

6 Chien, N., Wan Z.H., 1983. Mechanics of sediment transport. Science Press, Beijing, 101 pp.

7 Einstein, H.A., Chien, N., 1955. Effects of heavy sediment concentration near the bed on the velocity and sediment distribution. M.R.D. Sediment Series No.8, Missouri River Div., Corps Engrs., pp.76.

8 Farmer, D.M., Armi, L., 1986. Maximal two-layer exchange over a sill and through the combination of a sill and contraction with barotropic flow. Journal of Fluid Mechanics 164, 53-76.

9 Geyer, W. R., Ralston, D. K., 2015. Estuarine Frontogenesis. Journal of Physical Oceanography 45(2),546-561.

10 Huzzey, L.M., 1982.The dynamics of a bathymetrically arrested estuarine front. Estuarine, Coastal and Shelf Science 15(5), 537-552.

11 Largier, J.L., 1986. Structure and mixing in the Palmier Estuary, South Africa. South African Journal of Marine Science 4(1), 139-152.

12 Largier, J.L., Taljaard, S., 1991. The dynamics of tidal intrusion, retention and removal of seawater in a bar-built estuary. Estuarine, Coastal and Shelf Science 33(4), 325-338.

13 Largier, J. L., 1992. Tidal intrusion fronts. Estuaries 15(1), 26-39.

14 Li, B.G., et al., 1994. Report of topography and oceanography investigation for Liquified Petroleum Gas Terminal building in Liuheng. Second institute of oceanography, SOA, pp.42-48.

15 Nunes Vaz, R.A., Lennon, G.W., de Silva Samarasighe, J.R.,1989. The Negative role of turbulence in estuarine mass transport. Estuarine, coastal and shelf science 28,361-377.

16 Sutton, O.G., 1953. Micrometeorology, McGraw Hill Book Co, pp. 56~104.

17 Simpson, J. H., Hunter, J. R., 1974. Fronts in the Irish Sea. Nature 250, 404-406.

18 Simpson, J.H., Nunes, R.A., 1981. The tidal intrusion front: an estuarine convergence zone. Estuarine, Coastal and Shelf Science 13(3), 257-266.

19 Uncles, R.J., Stephens, J.A., 1997. Buoyancy phenomena in the Tweed Estuary. In: Aubrey, D., Friedrichs, C.T. (Eds.), Coastal and Estuarine Studies: Buoyancy Effects on Estuarine and Coastal Dynamics. AGU, Washington, DC, pp.175-193.

20 Uncles, R.J., 2011. Small-scale surface fronts in estuaries. Treatise on Estuarine and Coastal Science. 53-61.

21 Wang, X., Heron, M. L., Chen, W., 1998. On formation of tidal fronts in coastal seas. Journal of Hydrodynamics 3,17-28.

22 Yang, T.Z., et al., 2004. Report of topography and oceanography investigation for Zhoushan Coal base project (Liuheng port area). Second institute of oceanography, SOA, pp. 31-51.

23 Thain, R.H., Priestley, A.D., Davidson, M.A., 2004. The formation of a tidal intrusion front at the mouth of a macrotidal, partially mixed estuary: a field study of the Dart estuary, UK. Estuarine, Coastal and Shelf Science 61(1),161-172.